Validation of Numerical Model for Bubble Dispersion over a Hydrofoil

S. J. Zhu and A. Ooi
Department of Mechanical Engineering
Melbourne School of Engineering
The University of Melbourne
Victoria 3010, Australia

H. M. Blackburn
Department of Mechanical
and Aerospace Engineering
Monash University
Victoria 3800, Australia

B. Anderson
Maritime Platforms Divisions
Defence Science and
Technology Organisation
Victoria 3207, Australia

Abstract— **This study presents the direct numerical simulations (DNS) of bubbly wake flows. The DNS with Lagrangian particle dynamics (LPD) model is applied to the cases of bubble dispersion over a cylinder and a hydrofoil. The model validation is performed on the experimental data for the bubble behaviour in the wake of a circular cylinder. It is confirmed that the simulated distributions of bubble stream agree well with the trend of the measurement. The effect of angle of attack of a hydrofoil on the downstream bubble distribution is analysed. It is found that bubble stream deflection increases with increasing angle of attack. These results demonstrate that the joint DNS/LPD model can be applied to produce reasonably good results for the problem of bubbble dispersion over a hydrofoil.**

I. Introduction

The production and entrainment of bubbles in ship wakes is not completely understood despite the fact that it has many practical applications. For example, bubbles trapped in the large vortical structures in the ship wake can form clusters that are able to persist for large distances leaving a long trail of bubbles, which increases the ships echo and visual signatures; an important consideration in the defence environment. It is anticipated that with recent development of computer capability, understanding the behavior of bubbly flows by numerical simulation is becoming more common. The complicated behavior of bubbly propeller flow can be understood in a more fundamental manner by studying flow physics in hydrofoil wakes using direct numerical simulation (DNS) with a Lagrangian particle dynamics (LPD) method.

In dispersed bubbly flow, two types of models are prevalent, the Eulerian-Lagrangian (particle tracking) and the Eulerian-Eulerian (two-fluid) models. In the Eulerian-Lagrangian model, liquid is treated as a continuous phase that is described in the Eulerian mode, and bubbles are treated as a dispersed phase that is tracked in the Lagrangian mode. In the Eulerian-Eulerian model, the dispersed bubbles are treated as a second continuous phase intermingled and interacting with the continuous liquid phase based on the concept of volume averaging with different velocities and volume fractions for each phase.

Considering relatively small amounts of bubbles in the ship wakes, the method of Lagrangian particle tracking is most suitable for computing bubble distributions. It has advantages over the two-fluid model in the case of dilute suspensions or when large concentration variability of the discrete phase is present ([1], [2]). This situation is true for bubbly wake flows, such as those in ship wakes, where bubbles may experience preferential concentration and clustering effects in the near wake region but are rather dilute in the far wake [3]. The motivation for the Eulerian-Eulerian approach is that the Eulerian-Lagrangian approach requires considerable computational resources when the instantaneous trajectories of a large number of individual bubbles need to be calculated, where using Eulerian-Eulerian reduces significantly the required computation expenses ([4], [5]).

In summary, the Eulerian-Lagrangian models are sufficient if the bubble volume fraction is small, whereas Eulerian-Eulerian models are needed when the volume fraction is significant. Thus, the Eulerian-Lagrangian models are more suited for fundamental investigations of the bubbly flow [6] while Eulerian-Eulerian models are usually preferred in industrial simulations [7]. However, the Eulerian-Eulerian approach requires modelling of inter-phase forces, details of which remain uncertain. This paper thus discusses the validation of the numerical model for bubble dispersion over a hydrofoil.

II. Model Description

A. Numerical Methods for Incompressiobe flow

1) Governing Equations: The analytical techniques applied in this numerical study are associated with time-integration of the incompressible unsteady Navier-Stokes equations

$$\partial_t u = -N(u) - \frac{1}{\rho}\nabla p + \nu \nabla^2 u \quad (1)$$
$$\nabla \cdot u = 0 \quad (2)$$

where $u = u(x, y, z, t) = (u, v, w)(t)$ is the velocity field, $N(u)$ represents nonlinear advection terms, p, ρ and ν are respectively the fluid pressure, density and kinematic viscosity. The variables x, y, z and t are respectively the streamwise, vertical, spanwise and time coordinates and u, v, w are the velocity components in the streamwise, vertical and spanwise directions. The nonlinear terms are considered in skew-symmetric form $N(u) = (u \cdot \nabla u + \nabla \cdot uu)/2$.

978-1-4244-5222-4/10/$26.00 ©2010 IEEE

The velocity is assumed to be 2π-periodic in w, hence the velocity field can be projected exactly onto a set of two-dimensional complex Fourier modes

$$\hat{u}_k(x,y,t) = \frac{1}{2\pi}\int_0^{2\pi} u(x,y,z,t)exp(-ik\theta)d\theta, \qquad (3)$$

where k is an integer wavenumber. The velocity field can be recovered from these complex modes through Fourier series reconstruction

$$u(x,y,z,t) = \sum_{k=-\infty}^{\infty} \hat{u}_k(x,y,t)exp(ik\theta). \qquad (4)$$

In practice, only a finite number of modes are retained in the calculation, and the conjugate-symmetric property of the Fourier transforms of real variables is exploited, so that the negative-k modes are not required [8].

Equation (1) is subject to no-slip boundary conditions at the wall, a prescribed steady velocity at the inflow, conditions of zero pressure and zero outward normal derivatives of velocity at the outflow.

2) Spatial Discretization and Time Integration: Spatial discretization is carried out in a Cartesian coordinate system (Fig. 1), using standard nodal-Gauss-Lobatto-Legendre spectral element in the streamwise and vertical directions (x,y), and Fourier expansions in the spanwise direction (z) if required. This spatial discretization is coupled with a second-order-time velocity correction time-integration scheme.

The spectral element methods can deal with arbitrary geometric complexity, and are capable of local mesh adaption by either increasing the number of elements (h-refinement) or increasing the polynomial order within elements (p-refinement)[9]. It takes advantage of the favorable convergence properties (asymptotically exponential for smooth solution) of interpolation using families of orthogonal polynomials. These families can be characterized as polynomial eigenfunction solutions of singular Sturm-Liouville differential equations [8]. The Chebyshev and the Legendre polynomials are more commonly used among these eigenfunctions. In the spectral element method, it typically does not use these expansion functions directly, as they do not provide C^0 continuity across element boundaries; instead, it is the Gauss quadrature nodes and weights associated with the orthogonal polynomials that provide the linkage, and maintain the exponential convergence property [10]. Gauss-Lobatto quadrature nodes and weights are used in this case.

The use of Fourier expansions in the spanwise direction means that there is a one-to-one correspondence between wave number and Fourier mode index. As mentioned previously [11], by computing with the Fourier variables, solutions can retain the option of projecting back to full set of Fourier modes if required.

The time integration used is a projection scheme that based on backwards differecing in time. As originally described [12], this was characterized as an operator-splitting scheme, but

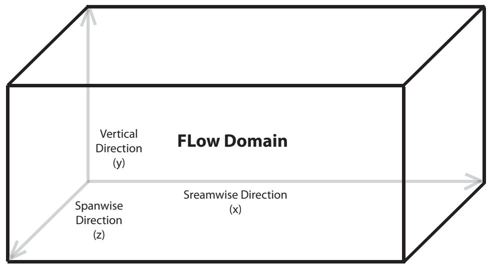

Fig. 1. Simulation domain and coordinate system.

more recently it has been shown that the method is one of a class of velocity-correction projection scheme [13]. To keep the overall account here reasonably brief, the reader is referred elsewhere [11] for a detailed description of the method and resolution studies as applied to DNS.

B. Simulation Conditions

Bubble dispersion over a cylinder and a hydrofoil at low Reynolds numbers (Re) are investigated. The Reynolds number is based on freestream velocity (U), cylinder diameter (d) or hydrofoil chord length (c), hence time scales are made dimensionless with respect to U/d and U/c respectively.

1) Cylinder: The flow field around the cylinder is modeled in two dimensions (Fig. 2) with the axis of the cylinder perpendicular to the direction of flow. The cylinder is modeled as a circle with a radius, $r = 1/2$ and a flow domain is created around the cylinder with the semi-circle inlet. The inlet and outlet boundaries are located at $10r$ upstream and $30r$ downstream. The width of the flow domain is $20r$.

A C-type grid of a cylinder is used and summarized by the arc ($\mathcal{C}$) and the dimension between the cylinder and the outer boundary ($\mathcal{N}$). The cell counts are 190×45 in these directions that is a total of $12,050$ elemental regions in the domain. In each element, two-dimensional mapped tensor-product Lagrange-interpolant shape functions based on the Gauss-Lobatto-Legendre nodes are applied. At $n_p = 5$ this elemental discretization corresponds to approximately $300,000$ local degrees of freedom in the domain.

A Dirichlet boundary condition of $u = (1,0,0)$ is applied at the inlet, top and bottom boundaries. A Neumann boundary condition of $\partial u/\partial n = 0$ is applied at the outlet, where n is the outward normal direction to the boundary.

2) Hydrofoil: The flow field around a NACA 0012 hydrofoil with chord length, $c = 1$, at a angle of attack (α) can be modeled in the similar fashion of the cylinder model (Fig. 3). The circular inlet and outlet boundaries are located at $5c$ upstream and $10c$ downstream. The width of the flow domain is $10c$.

The same C-type grid is used around the hydrofoil and summarized by the arc ($\mathcal{C}$), the dimension between the airfoil and the outer boundary ($\mathcal{N}$). The cell counts are 218×35 in these directions. A total of $7,630$ elemental regions in the domain are created. In each element, two-dimensional mapped tensor-product Lagrange-interpolant shape functions

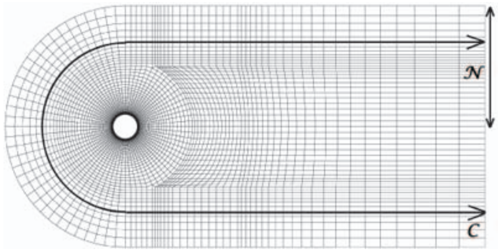

Fig. 2. Cylinder domain.

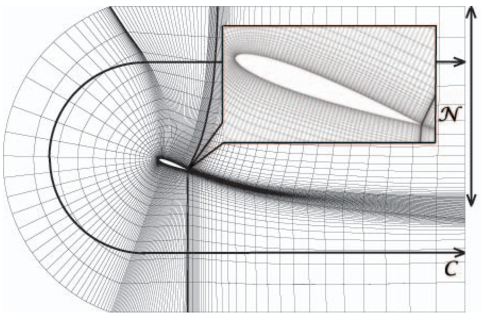

Fig. 3. Hydrofoil domain.

based on the Gauss-Lobatto-Legendre nodes are applied. At n_p = 5 this elemental discretization corresponds to approximately $190,000$ local degrees of freedom in the domain. The grid in proximity to the hydrofoil is also illustrated in Fig. 3.

Similarly, a Dirichlet boundary condition of $u = (1, 0, 0)$ is applied at the inlet, top and bottom boundaries. A Neumann boundary condition of $\partial u/\partial n = 0$ is applied at the outlet.

C. Bubble Tracking Formulation

Bubbles in the flow are experiencing the combined effects of the carrying fluid flow and the buoyancy force. Thus, a precise force balance acting on the bubbles is required. The bubble trajectories are obtained using the equation of motion from [14] as it was obtained from the experimental data on bubble dynamics in vortex flows, similar to those of bubbly wake flows.

$$\frac{dU_b}{dt} = A_a + A_b + A_d + A_l \tag{5}$$

where U_b is the bubble velocity and A_a, A_b, A_d and A_l are the accelerations due to added mass, buoyancy, drag and lift respectively.

Added mass: It is also known as virtual mass, which is the inertia added to a bubble as it is accelerating or decelerating in the fluid. The acceleration due to added mass is

$$A_a = C_a \left(\frac{\partial U_f}{\partial t} + (U_f \cdot \nabla) U_f \right) \tag{6}$$

where U_f is the fluid velocity and the coefficient of added mass (C_a) is found to be 3.0, provided the bubble is nearly spherical [14].

Buoyancy: The acceleration due to buoyancy is

$$A_b = -C_b g \tag{7}$$

where g is the gravity and the coefficient of bouyancy (C_b) is found to be 2.0 [14].

Drag: Acceleration due to drag is

$$A_d = \frac{3}{4r_b} C_d \left| U_{rel} \right| U_{rel} \tag{8}$$

where r_b and U_{rel} are respectively the bubble radius and relative velocity between the bubble and fluid. The coefficient of drag (C_d) can be taken from the empirical drag relatioship [15]

$$C_d = \left[\frac{1}{(\varphi_1 + \varphi_2)^{-1} + (\varphi_3)^{-1}} + \varphi_4 \right]^{1/10} \tag{9}$$

where

$$\begin{aligned} \varphi_1 &= (24 Re_b^{-1})^{10} + (21 Re_b^{-0.67})^{10} \\ &\quad + (4 Re_b^{-0.33})^{10} + (0.4)^{10} \end{aligned} \tag{10}$$

$$\varphi_2 = \frac{1}{(0.148 Re_b 0.11)^{-10} + (0.5)^{-10}} \tag{11}$$

$$\varphi_3 = (1.57 \times 10^8 Re_b^{-1.625})^{10} \tag{12}$$

$$\varphi_4 = \frac{1}{(6 \times 10^{-17} Re_b^{2.63})^{-10} + (0.2)^{-10}} \tag{13}$$

and Re_b is the Reynolds number based on bubble relative velocity (U_{rel}) and bubble diameter (d_b)

$$Re_b = \frac{\left| U_{rel} \right| d_b}{\nu} \tag{14}$$

The relationship is calibrated free of systematic error with experimental data available for $Re_b < 10^6$.

Lift: Acceleration due to lift is

$$A_l = \frac{3}{4r_b} C_l \left| U_{rel} \right|^2 \frac{U_{rel} \times \vec{\omega}}{\left| U_{rel} \right| \left| \vec{\omega} \right|} \tag{15}$$

where the coefficient of lift (C_l) was derived to be 0.53 [16] and $\vec{\omega}$ is the vorticity

$$\vec{\omega} = 0.5 * (\nabla \times U_f) \tag{16}$$

Bassett force: The bassett force term involves a history integral of the interactions of a bubble with its own wake that is expected to be much smaller than the other dominant forces acting on bubbles [17]. The contribution of the Bassett force was concluded to be less than 6% of the bouyancy force [14]. Consequently this force is neglected in this study.

III. Experimental Data

The experimental work of bubble behaviour in the wake of a circular cylinder was conducted previously [18]. In the experiments, the flow is generated by the Kelly & Lewis Model 50 Series 1 water pump. An ABB pump controller is used to adjust the water flow rate to achieve different Reynolds numbers. Air bubbles are injected through a nozzle at the bottom of the water tunnel. The size of bubble can be controlled by adjusting the air flow rate using a valve. A cylinder with a diameter 27 mm is mounted on the cylinder holder. Bubbles of 2 mm in diameter are injected through the nozzle at upstream.

It is found that bubble stream forms the characteristic "S" shape in the wake region beind the cylinder. At $Re = 6610$ (Fig. 5(a)), the bubble stream is attracted back towards the near wake region as it passes the bottom point of the cylinder. The bubble stream moves back ward and bounces off the cylinder as it continues to move vertically up before reaching the freestream. At $Re = 7430$ (Fig. 5(b)), the increasing freestream velocity pushes the bubbles further downstream before encountering the wake region. On reaching the wake region, the bubbles turn back while moving upward. As bubbles reach the upper boundary of the wake region, they begin to turn in the direction of the freestream to form the "S" shape. At $Re = 8600$ (Fig. 5(c)), the bubble stream continues to follow the behaviour identified at Reynolds number of 7430. However, the increased freestream velocity casues the "S" to bend sharper. At $Re = 9560$ (Fig. 5(d)), the bubbles show clear signs of capture. The bubbles are being pushed downward as they turn in the direction of the freestream to form bubble packets entrained in the vortices behind the cylinder.

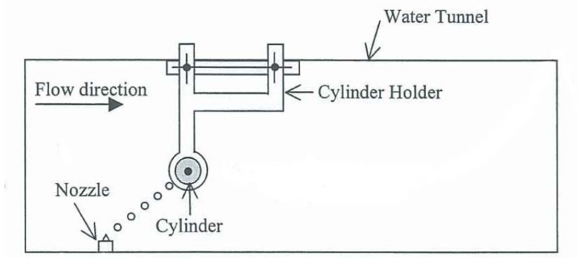

Fig. 4. Experimental setup for bubble dispersion over a cylinder [18].

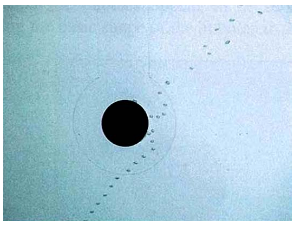

(a) $Re = 6610$

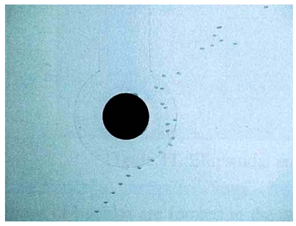

(b) $Re = 7430$

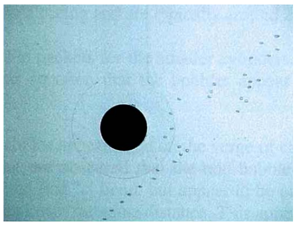

(c) $Re = 8600$

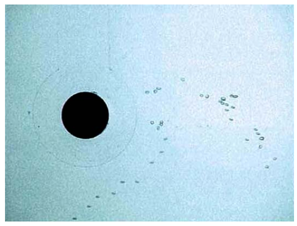

(d) $Re = 9560$

Fig. 5. Bubble behaviour in the wake of a circular cylinder showing the "S" shape [18].

IV. Results

A. Validation on Bubble Dispersion over a Cylinder

The validation of the DNS/LPD model is performed on the experimental data of bubble behaviour in the wake of a circular cylinder [18] (Fig. 4).

Simulations of bubble dispersion over a cylinder at two different Reynolds numbers ($Re = 200$ and 400) are conducted. Simulations start in the two-dimensional flow domain and bubbles are not initiated until the flow field reaches periodic shedding. A time step of $h = 0.0001$ is used and a total of 200 bubbles with the similar length scale as the experimental case are continuously released with an interval of 100 time steps. Bubbles are released below the cylinder near wake region as they will not be carried from upstream to downstream at low Reynolds numbers. Fig. 6 shows the instantaneous bubble distributions with the spanwise vorticity contour (ω_z) computed by DNS/LPD model. It can be seen that the characteristic "S" shape identified in the experiments is captured in the simulaiton results. The formation of the "S" shape can be explained by the combined effects of the vortices developed at the back of the cylinder. The bubble stream is firstly drawn back towards the near wake region behind the cylinder due to the influence of the lower vortex that is in the anticlockwise direction. Then, it is pushed back into the direction of freestream due to the influence of the upper vortex that is in the clockwise direction. However, bubble entrainment is not captured in the current simulations as the Reynolds numbers is not sufficiently high enough compared to the experimental condition.

B. Bubble Dispersion over a Hydrofoil

Six bubble dispersion cases at two different angles of attack ($\alpha_1 = 10°$ and $\alpha_2 = 20°$) and three different Reynolds numbers ($Re = 200$, 450 and 800) have been performed and the results are presented in Fig. 7. Simulations still start in the two-diemnsional flow domain and bubbles are not initiated until the flow field reaches steady state or periodic shedding. The same time step of $h = 0.0001$ is used and a total of 300 bubbles are continuously released below the hydrofoil with an interval of 200 time steps.

Similar dynamic features found in the cylinder simulations are also identified in the hydrofoil data. In all cases, bubble stream rises up towards the wake region behind the hydrofoil.

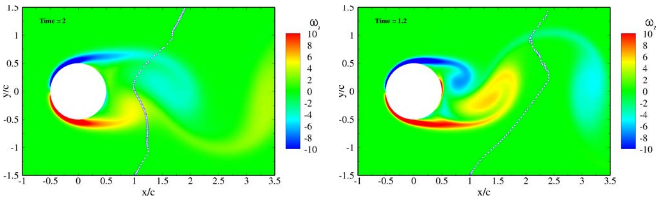

(a) $Re = 200$ (b) $Re = 400$

Fig. 6. Bubble dispersion in the wake of a cylinder with the spanwise vorticity contour ω_z.

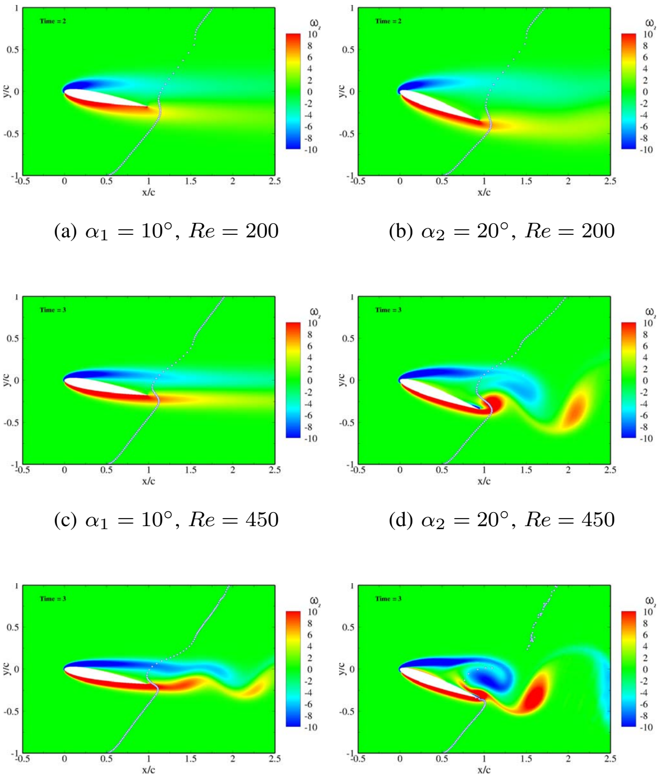

(a) $\alpha_1 = 10°$, $Re = 200$ (b) $\alpha_2 = 20°$, $Re = 200$

(c) $\alpha_1 = 10°$, $Re = 450$ (d) $\alpha_2 = 20°$, $Re = 450$

(e) $\alpha_1 = 10°$, $Re = 800$ (f) $\alpha_2 = 20°$, $Re = 800$

Fig. 7. Effects of angle of attack and Reynolds number on bubble distribution with the spanwise vorticity contour ω_z.

As it reaches the bottom of the wake region, bubbles turn back towards the trailing edge of the hydrofoil while moving upwards due to the influence of the lower vortex. As it reach the upper half of the wake region, bubbles turn into the direction of freestream due to the influence of the upper vortex. Thus, bubble stream forms the characteristic “S” shape. At an angle of attack of 10°, flow is steady at Reynolds numbers of 200 and 450 (Fig. 7(a) and 7(c)). Hence, the “S” shape is stationary in both cases. As shown in Fig. 7(e)), weak unsteady vortex shedding developed at the back of the hydrofoil at Reynolds number of 800 causes the “S” shape to oscillate slowly in the wake region. After increasing the angle of attack to 20°, both flow and bubble stream remain steady at Reynolds number of 200 (Fig. 7(b)). Flow starts to become unsteady at Reynolds number of 450 (Fig. 7(d)) and strong periodic shedding is observed behind the hydrofoil casuing bubble stream to oscillate severely in the wake region. As Reyonlds number increases to 800 (Fig. 7(f)), it is found that the bubble stream is oscillating and being broken up periodically by the stronger vortices developed from the hydrofoil. No bubble capture is observed with the current simulation data. However, bubbles are found to be entrained into the vortices developed at the trailing edge of the hydrofoil. As the vortices become weaker as it convects downstream, bubbles eventually escaped from them due to the effect of buoyancy force.

V. Conclusions and Future Work

The results of this study show the joint DNS/LPD model is applicable for computing the bubble dispersion over a hydrofoil at low Reynolds numbers. Bubble distribution in the cylinder and hydrofoil wakes are obtained and the characteristic dynamical features are observed in the computed results. To further improve the current bubble model, a joint large eddy simulation (LES) and LPD method is proposed to simulate bubble distribution at higher Reynolds numbers.

References

[1] S. Elghobashi, “On predicting particle-laden turbulent flows”, *Appl. Sci. Res.*, vol.52, pp.309-329, 1994.

[2] C. T. Crowe, “An assessment of multiphase flow models for industrial applications”, in *Proc. FEDSM’98*, vol.FEDSM-5093, Washington, DC, USA, 1998.

[3] A. Smirnov, I. Celik, and S. Shi, “LES of bubble dynamics in wake flows”, *Comput. Fluids*, vol.34, pp.351-373, 2005.

[4] O. A. Druzhinin and S. Elghobashi, “Direct numerical simulations of bubble-ladden turbulent flow using the two-fluid formulation”, *Phys. Fluids*, vol.10, No.3, pp.685-697, 1998.

[5] O. A. Druzhinin and S. Elghobashi, “A Lagrangian-Eulerian mapping solver for direct numerical simulation of bubble-laden turbulent shear flows using the two-fluid formulation”, *J. Comput. Phys*, vol.154, pp.174-196, 1999.

[6] Y. Pan, M. P. Dudukovic, and M. Chang, “Dynamic simulation of bubbly flow in bubble columns”, *Chem. Eng. Sci.*, vol.54, No.13, pp.2481-2489, 1999.

[7] L. M. Portela and R. V. A. Oliemans, “Possibilities and limitations of computer simulations of industrial turbulent dispersed multiphase flows”, *Flow Turbul. Combust.*, vol.77, pp.381-403, 2006.

[8] C. Canuto, M. Y. Hussaini, A. Quarteroni, and T. A. Zang, “Spectral methods in fluid dynamics”, 2nd ed. Berlin: Springer, 1988.

[9] R. D. Henderson, “Adaptive spectral element methods for turbulence and transition”, *In High-order methods for computational physics* (T. J. Barth and H. Deconinck, ed.), Berlin: Springer, pp.225-324, 1999.

[10] H. M. Blackburn and S. Schmidt, “Spectral element filtering techniques for large eddy simulation with dynamic estimation”, *J. Comput. Phys.*, vol.186, pp.610-629, 2003.

[11] H. M. Blackburn and S. J. Sherwin, “Formulation of a Galerkin spectral element-Fourier method for three-dimensional incompressible flows in cylindrical geometries”, *J. Comput. Phys.*, vol.197, pp.759-778, 2004.

[12] G. E. Karniadakis, M. Israeli, and S. A. Orszag, "Higher-order splitting methods for incompressible Navier-Stokes equations”, *J. Comput. Phys.*, vol.97, No.2, pp.414-443, 1991.

[13] J. Guermond and J. Shen, "Velocity-correction projection methods for incompressible flows”, *SIAM Journal on Numerical Analysis*, vol.41, No.1, pp.112-134, 2003.

[14] G. Sridhar and J. Katz, "Darg and lift forces on microscopic bubbles entrained by a vortex”, *Phys. Fluids*, vol.7, No.2, pp.389-399, 1995.

[15] J. Almedeij, "Drag coefficient of flow around a sphere: Matching asymptotically the wide trend”, *Powder Technology*, vol.186, pp.218-223, 2008.

[16] T. R. Auton, "The dynamics of bubbles, drops and particles in motion in liquids", *Ph.D. Thesis*, Cambridge University, Cambridge, UK, 1981.
[17] V. V. Ranade, "Computational flow modelling for chemical reactor engineering", *Academic Press*, London, 2002.
[18] P. Tho, S. Vassallo, A. Ooi, and R. Manasseh, "Bubble behaviour in the wake of circular cylinders", *Final Year Research Project*, The University of Melbourne, Melbourne, Australia.